Chapter 17
Applicability of Time-Averaged Holography for Reliability Assessment of Chemical Sensors

P. Palevičius, M. Ragulskis, and A. Palevičius

Abstract This paper investigates applicability of time-averaged holography for reliability assessment of chemical sensors operating in dynamic mode. Time-averaged holography, which is an experimental method for quantitative registration of surface oscillations, is applied for computational results of a paradigmatic cantilever chemical sensor model for various excitation parameters. It is shown that even a harmonic excitation of a non-linear microsystem may result into an unpredictable chaotic motion. The results show that a straightforward interpretation of time-averaged holographic interferograms of chemical sensors can be misguiding.

17.1 Introduction

Interferometry and holographic interferometry are powerful optical methods for mapping changes in the shape of three-dimensional objects with high accuracy. These methods are used for nondestructive testing, analysis of profiles of surfaces, detection of deflections, motion, structural vibrations in microsystems where the amplitudes of those vibrations are in the range of nanometers to a few micrometers [1–6] and [7]. An overview of a large variety of its applications for MEMS characterization, residual stress measurement, design and evaluation, and device testing and inspection is given in [8]. Digital holography and speckle interferometry are also widely used for the quality inspection and the assessment of reliability

P. Palevičius (✉) • M. Ragulskis
Department of Mathematical Modeling, Kaunas University of Technology,
Studentu st. 50-146, LT-51368 Kaunas, Lithuania
e-mail: paulius.palevicius@ktu.lt; minvydas.ragulskis@ktu.lt

A. Palevičius
Faculty of Mechanical Engineering and Design, Kaunas University of Technology,
Studentu st. 56, LT-51424 Kaunas, Lithuania
e-mail: arvydas.palevicius@ktu.lt

J. Bonča and S. Kruchinin (eds.), *Nanotechnology in the Security Systems*,
NATO Science for Peace and Security Series C: Environmental Security,
DOI 10.1007/978-94-017-9005-5_17,

of microsystems. These optical techniques are employed for the measurement of displacements, deformations induced by mechanical, thermal, or electrostatic loads [9, 10].

Time average holography is an experimental method for quantitative registration of surface oscillations which has been widely applied for the investigation of microsystems. The application of this method has been employed in dynamic micrometrology [11], dynamic characterization of MEMS diaphragm [12], measurement of static and vibrating microsystems [13].

One of the assumptions made when applying time-average holography method is that oscillations are harmonic which might not be the case in real life applications of microsystems. It is well known that even a periodic excitation of non-linear system may result into unpredictable chaotic behavior. Nonlinear and chaotic effects in microsystems are widely investigated in [14–17].

One of the common microsystem devices is a chemical senor. The cantilever beam chemical sensor consists of two key components: a gas sorptive layer, such as a polymer, and the cantilever beam transducer. There are two modes of operation of the cantilever beam that can be distinguished [18]. In the static mode, the bending of the cantilever beam upon mass loading and related surface stress is measured. In the dynamic mode, the cantilever beam can be actuated at its fundamental resonant frequency. The fundamental resonant frequency in turn depends on the mass loading of the cantilever beam. In this article a paradigmatic cantilever chemical sensor model is used to illustrate the formation of time-averaged holographic fringes when the sensor performs complex transient oscillations.

17.2 Optical Background

The basic principle of the formation of time-averaged holographic interference fringes can be illustrated by the harmonically oscillating cantilever beam. Let us assume that the harmonic vibration of the beam is defined as

$$Z\,(x)\sin\omega t, \tag{17.1}$$

where t is time; x is the longitudinal coordinate of the beam; $Z\,(x)$ is transverse amplitude of oscillations of the one-dimensional beam at coordinate x; ω is the frequency of harmonic oscillations. Then the characteristic function defining the complex amplitude of the laser beam M_T in the plane of the hologram takes the form [19]:

$$M_T = \lim_{T\to\infty}\frac{1}{T}\int_0^T \exp\left(i\left(\frac{4\pi}{\lambda}\right)Z\,(x)\sin\omega t\right)dt = J_0\left(\left(\frac{4\pi}{\lambda}\right)Z\,(x)\right), \tag{17.2}$$

where T is the exposure time of the hologram, $(T \gg 1/\omega)$; λ is the laser wavelength; and J_0 is the zero order Bessel function of the first kind. Then, the resulting intensity I of the point (x, y) on the hologram is

$$I(x, y) = a^2(x, y)\,|M_T|^2, \tag{17.3}$$

where $a(x, y)$ is the distribution of the amplitude of the incident laser beam. Note that the decay of gray-scale intensity is rather fast at increasing amplitudes of oscillation. Better visualization of higher order time-averaged fringes requires contrast enhancement of the time-averaged image. As a limited number of intensity levels is used for the digital representation of images a sigmoid mapping function can be used to distort the intensity scale for better visualization of the results of calculations. The enumerated time-averaged holographic fringes are then used for reconstruction of the field of amplitudes of harmonic oscillations. The amplitude of harmonic oscillations at point x_k corresponding to centerline of the k-th time-averaged holographic fringe equals to:

$$Z(x_k) = \lambda r_k / 4\pi, \tag{17.4}$$

where r_k; $k = 1, 2, \ldots$ is the k-th root of the zero order Bessel function of the first kind.

All calculations in the following sections are based on the assumption that the illumination and the observation directions are perpendicular to the plane of the beam in the state of equilibrium (in the par-axial model).

17.3 Cantilever Beam Model

As mentioned in the introduction we will use cantilever beam model for the computational experiment illustrating the formation of time-averaged holographic fringes when the cantilever performs complex transient oscillations. A schematic diagram of a typical MEMS device comprising a deformable beam over a fixed ground electrode is shown in Fig. 17.1. Potential difference is applied between the beam and the ground electrode which induces electrostatic charges. These two electrostatic charges creates electrostatic pressure normal to the surface of conductor.

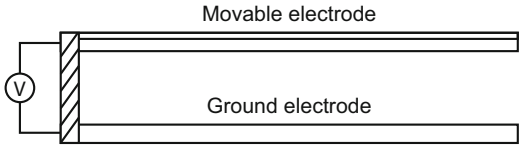

Fig. 17.1 The schematic diagram of the MEMS device – a beam with an applied voltage V over a ground plane

Finite element method (FEM) is used for the simulation of this MEMS device. Time-dependent simulation is implemented in COMSOL Multiphysics package.

A material used for the beam structure is Silicon with relative permittivity $\epsilon = 11.7$, density $\rho = 2329\,\mathrm{kg/m^3}$, Young's modulus $E = 170e9\,\mathrm{Pa}$ and Poisson's ratio $\nu = 0.28$. The polysilicon is assumed to be heavily doped, so that electric field penetration into the structure can be neglected. The beam resides in an air-filled chamber that is electrically insulated. The dimensions of the beam are: Length 200 μm; Depth 20 μm; and Height 2 μm. The model considers a layer of air 10 μm thick above and 10 μm thick to the sides of the beam, and the air gap between the bottom of the beam and the grounded plane is initially set to 2 μm. The cantilever is coated with a thin layer of sorptive polymer that allows the resonating cantilever to detect analyte concentrations in the environment [20].

Electromechanics physics Comsol interface is used for computational simulation. It combines solid mechanics and electrostatics with a moving mesh to model the deformation of electrostatically actuated structures:

$$\rho \frac{\partial^2 u}{\partial t^2} - \nabla \cdot \sigma = F v, \tag{17.5}$$

$$\nabla \cdot D = \rho_v, \tag{17.6}$$

here u denotes the displacement field; t is time; ρ is the material density; σ is the stress tensor; F is an external volume force; D is electric displacement or electric flux density; v is velocity and ρ_v is charge density in vacuum.

An electrostatic force caused by the potential difference between the two electrodes bends the beam toward the grounded plane beneath it. This model calculates the electric field in the surrounding air in order to compute the electrostatic force. As the beam bends, the geometry of the air gap changes continuously, resulting in a change in the electric field between the electrodes. The coupled physics is handled automatically by the Comsol electromechanics interface.

The electrostatic field in the air and in the beam is governed by Poisson's equation:

$$-\nabla \cdot (\varepsilon \nabla V) = 0, \tag{17.7}$$

where derivatives are taken with respect to the spatial coordinates. The force density that acts on the electrode of the beam results from Maxwell's stress tensor:

$$F_{es} = -\frac{1}{2}(E \cdot D)\, n + (n \cdot E)\, D, \tag{17.8}$$

where E and D are the electric field and electric displacement vectors and n is the outward normal vector of the boundary. Note that this force is always oriented along the normal of the boundary.

A condition of the zero charge on the boundary is used as this is the default boundary condition at exterior boundaries.

$$-n \cdot D = 0. \tag{17.9}$$

The initial values for electric potential and solid displacement field are:

$$u|_{t=0} = 0, \; V|_{t=0} = 0. \tag{17.10}$$

The fixed constraint condition that makes the geometric entity fixed (the displacements are zero in all directions) are applied to the edges of the beam. Ground boundary condition is applied to the bottom plain which gives zero potential on the boundary. The boundary condition is applied to the beam of an electric potential V_0.

$$V = V_0. \tag{17.11}$$

17.4 Computational Experiment

Computational simulation is performed for the model of cantilever beam (the model is described in details in Sect. 17.3) with three different electric potential boundary conditions. In order to simplify the visualization of transient processes we select a single point at the center of the cantilever beam (where the displacements are largest) and plot time signals and phase diagrams for all three different potential boundary conditions (Fig. 17.2).

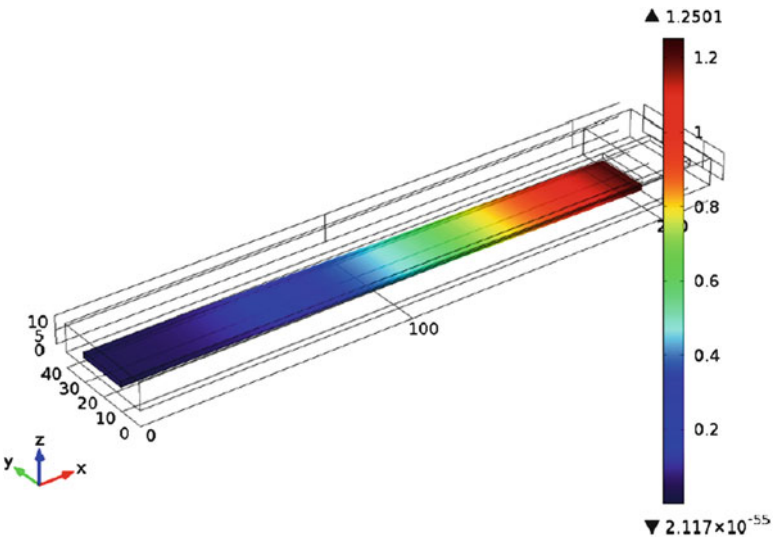

Fig. 17.2 The shape of the cantilever in the state of maximum deformation while performing periodic oscillations according to the first computational experiment

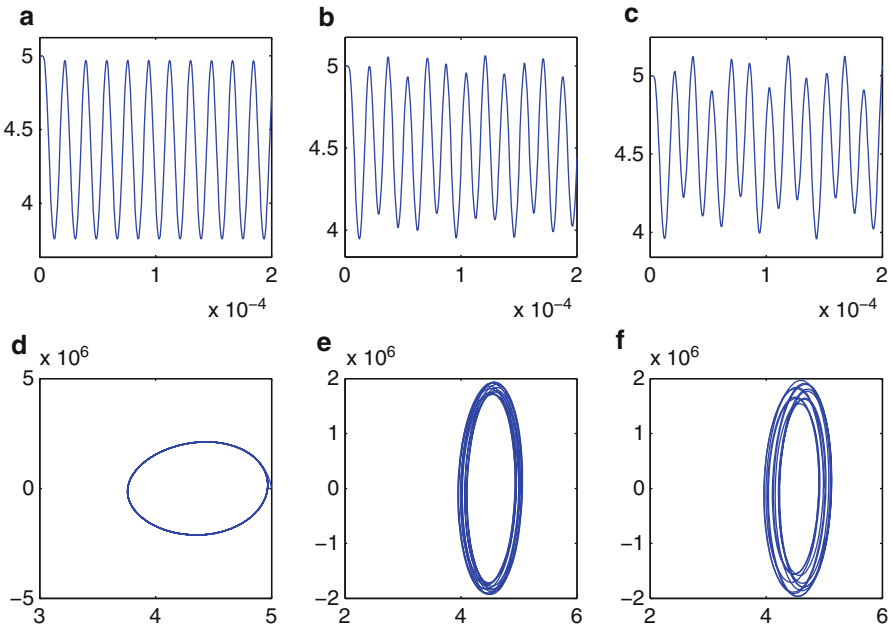

Fig. 17.3 Results of simulations illustrating the dynamics of central node of the cantilever. Parts (**a**) and (**b**) show the transient process in time and in phase diagram when the micro-device is excited according to the first computational experiment. Parts (**c**) and (**d**) ((**e**) and (**f**)) illustrate the results of the second (the third) computational experiments

During the first computational experiment (i) a DC (direct current) bias of $V_{DC} = 23\,\mathrm{V}$ is applied to the micro-device in order to obtain the system's response. The DC bias is applied using the standard Comsol smoothed step function which allows to increase the voltage incrementally from 0 to V_{DC} during the transient interval ranging from 0 to $6e-6$. After the transient interval the DC bias is set to a constant:

$$V = V_{DC}. \tag{17.12}$$

The second computational experiment (ii) employs a DC bias on top of a sinusoidal AC voltage:

$$V = V_{DC} + V_{AC} \sin(2\pi f t), \tag{17.13}$$

where $V_{DC} = 21\,\mathrm{V}$ and $V_{AC} = 0.75\,\mathrm{V}$. Finally, a DC bias of $V_{DC} = 20\,\mathrm{V}$ with AC voltage of $V_{AC} = 2\,\mathrm{V}$ is applied in the last computational experiment (iii). The exposure time t used in all simulations is ranging form 0 to $2e-4$ with a time step of $2e-7\,\mathrm{s}$.

The results of computational experiments are presented in Fig. 17.3. It can be seen that the response of the system is periodic under the constant DC bias

excitation. Note that these periodic oscillations are caused not by a harmonic excitation – the cantilever is deflected from the state of equilibrium during the short transient process and continues to oscillate because the damping is small (mass damping parameter $\alpha_{dM} = 418.9$ 1/s and stiffness damping parameter $\beta = 8.29e - 13$ s).

The results of the second computational experiment are different compared to the periodic oscillation caused by the short DC transient in the first computational experiment. The harmonic AC component interacts with the natural frequency of the cantilever – the resultant process of oscillations is no longer periodic (Fig. 17.3c, d). Finally, the response of the system to last excitation is clearly nonlinear. The attractor in the phase plane diagram looks like a chaotic attractor even in a relatively short observation window (Fig. 17.3f).

17.5 Computational Reconstruction of Time-Averaged Holographic Fringes

Time-averaged holographic fringes illustrated in Fig. 17.1 are based on the assumption that structure performs harmonic oscillations. Dynamics analysis of the cantilever MEMS shows that transient processes can be very complex. Even in the most simple case periodic oscillations of the cantilever are not harmonic. This fact requires a separate analysis of processes governing the formation of time-averaged holographic fringes in the hologram plane.

17.5.1 Computational Reconstruction of Time-Averaged Holographic Fringes

The characteristic function defining the complex amplitude of the laser beam M_T when the according surface point performs oscillations defined by function $\xi(t)$ reads:

$$M_T = \lim_{T\to\infty} \frac{1}{T} \int_0^T \exp\left(\imath \frac{4\pi}{\lambda} \xi(t)\right) dt =$$

$$= \lim_{T\to\infty} \frac{1}{T} \int_0^T \cos\left(\frac{4\pi}{\lambda} \xi(t)\right) dt + \imath \lim_{T\to\infty} \frac{1}{T} \int_0^T \sin\left(\frac{4\pi}{\lambda} \xi(t)\right) dt == R_c + \imath R_s. \tag{17.14}$$

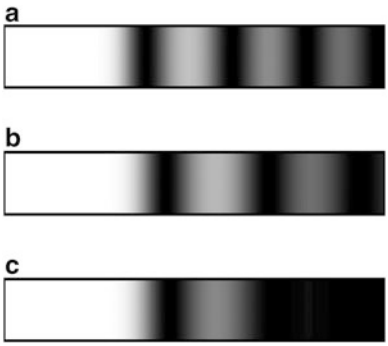

Fig. 17.4 The formation of interference fringes for computational experiments (i), (ii) and (iii)

Note that when $\xi(t) = Z\sin(\omega t)$ the complex part R_s tends to zero because integrant is an odd function. Then M_T can be computed as an arithmetic average over discrete time steps in a period of harmonic oscillations:

$$M_T = \lim_{T\to\infty}\frac{1}{T}\int_0^T \cos\left(\frac{4\pi}{\lambda}Z\sin(\omega t)\right)dt = \\ = \lim_{n\to\infty}\sum_{k=1}^{n}\cos\left(\frac{4\pi}{\lambda}Z\sin\left((k-1)\frac{2\pi}{k}\right)\right)dt = J_0\left(\frac{4\pi}{\lambda}Z\right). \quad (17.15)$$

But when oscillations are defined by a non-harmonic function $\xi(t)$ R_s does not converge to zero and the gray-scale level in the hologram plane reads (assuming that $a^2(x, y) = 1$):

$$|M_T|^2 = R_c^2 + R_s^2. \quad (17.16)$$

In practice one needs to compute arithmetic averages of R_c and R_s over a sufficiently long set of discrete points in the exposure time interval.

It is well known that a non-linear system with a harmonic load may exhibit complex chaotic solutions. The theoretical results that intensity level of interference bands decrease are discussed in [21].

17.5.2 The Formation of Interference Fringes

So far the dynamics of the central point of the cantilever is discussed (where the deflections from the state of equilibrium are largest). In order to visualize the dynamic of the whole surface of the cantilever we will use whole field Time-Averaged holography simulation techniques (Fig. 17.4).

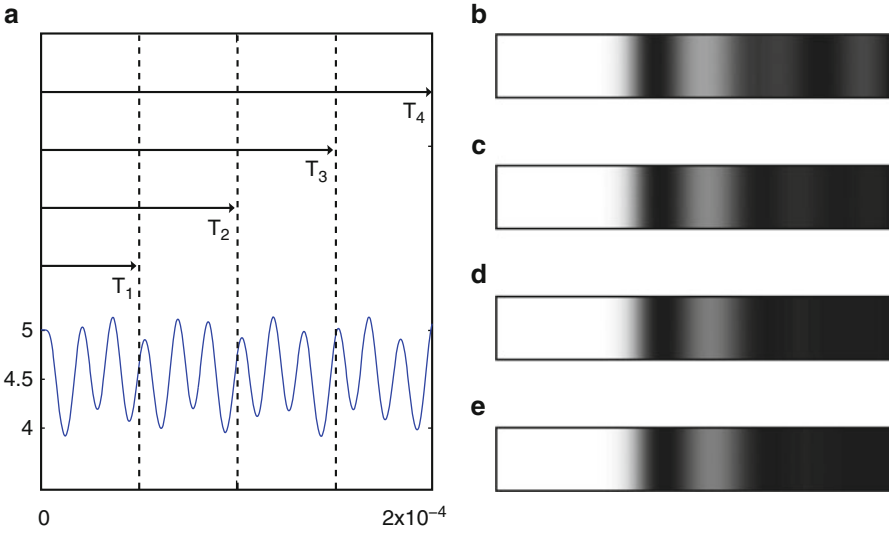

Fig. 17.5 Computational experiment (iii) divided into four time intervals. The formation of interference fringes for time intervals (T1), (T2), (T3), (T4) are given in parts (**b**), (**c**), (**d**), (**a**)

FEM modeling yields complete data on the dynamics of the cantilever – distances between the beam plane and the ground plane are available from the simulation results for all time steps. The method described in the Sects. 17.2 and 17.5.1 will be applied for the data produced by all three computational experiments. Equation (17.3) is used for each point on the plane in order to determine the gray-scale level in time-averaged hologram. Laser wavelength used for calculation is set to $\lambda = 632.8\,\text{nm}$. Other parameters are set to $I_L = 1$; $k_d = 1$; $k_s = 0$. Note that we model a non-specular surface of the cantilever.

Numerically reconstructed time-averaged holograms generated by the cantilever according to the computational experiments (i), (ii) and (iii) are illustrated in parts (a), (b) and (c) in Fig. 17.5. Note that time-averaged fringes in part (b) are less developed compared to part (a). This can be explained by a much more complex transient process the cantilever is experiencing under excitation (ii). It is almost impossible to observe time averaged fringes in part (c) – complex chaotic oscillations do not generate time-averaged holographic fringes.

17.5.3 Interference Fringes Induced by Different Time Intervals of Chaotic Oscillation

The situation becomes even more complex when the oscillation is not periodic but is chaotic. As mentioned previously chaotic oscillations do not generate time-averaged

holographic fringes. But this result holds when exposure time tends to infinity. Finite exposure times result into interpretable patterns of fringes even for chaotic oscillations.

We use the same data produced by computational experiment (iii) but construct time-averaged holograms for different exposure times. Time-averaged holograms for exposure times T_1, T_2, T_3 and T_4 are illustrated in Fig. 17.5. A gradual loss of the time-averaged fringes can be observed as exposure time increases. That suggests another important conclusion. A straightforward identification of the motion law from time-averaged holographic fringes is prone to severe errors if the motion law of the investigated structure is not known. A short exposure time over a chaotic motion (Fig. 17.5b) suggests a harmonic oscillation of the cantilever – though this is completely not true. Another important conclusion follows from Fig. 17.5e. One should not blame his optical setup if the generated time-averaged hologram does not yield a pattern of fringes. The optical setup may be in perfect order – simply the structure may be oscillating according to a chaotic law.

17.6 Conclusions

Time averaged holography is a powerful optical experimental technique for reliability assessment of chemical sensors operating in dynamic mode. The inverse problem for the interpretation of time-averaged holographic fringes is a well defined and straightforward task if only the oscillations of the investigated structures are harmonic. It is demonstrated that complex chaotic motions can be generated even in rather simple micro-electromechanical systems such as chemical sensors. Therefore a straightforward interpretation of time-averaged holographic interferograms of micro-mechanical components can be not only be misguiding but the experimental holographic images may not reveal any interpretable fringes at all as chaotic oscillations do not generate time-averaged holographic fringes. Thus one needs to make sure that the response of the excited chemical sensors is not chaotic before questioning the functionality of the optical experimental setup.

References

1. Krishna Mohan N, Rastogi PK (2009) Recent developments in interferometry for microsystems metrology. Opt Lasers Eng 47(2):199–202
2. Kujawinska M (2002) Modern optical measurement station for micro-materials and micro-elements studies. Sens Actuators A Phys 99(1–2):144–153
3. Salbut L, Kacperski J, Styk AR, Jozwik M, Gorecki C, Urey H, Jacobelli A, Dean T (2004) Interferometric methods for static and dynamic characterizations of micromembranes for sensing functions. In: Proceedings of SPIE, photonics Europe 2004, optical micro- and nanometrology in manufacturing technology, MEMS characterization I, Tome 5458, 29–30 April 2004, pp 16–24

4. Yang L, Schuth M, Thomas D, Wang Y, Voesing F (2009) Stroboscopic digital speckle pattern interferometry for vibration analysis of microsystem. Opt Lasers Eng 47(2):252–258
5. De Pasquale G (2013) Experimental analysis of viscous and material damping in microstructures through the interferometric microscopy technique with climatic chamber. J Sound Vib 332(18):4103–4121
6. Krupa K, Gorecki C, Jozwicki R, Jozwik M, Andrei A (2011) Interferometric study of reliability of microcantilevers driven by AlN sandwiched between two metal layers. Sens Actuators A Phys 171(2):306–316
7. Koev ST, Bentley WE, Ghodssi R (2010) Interferometric readout of multiple cantilever sensors in liquid samples. Sens Actuators B Chem 146(1):245–252
8. Asundi A (2011) Digital holography for MEMS and microsystem metrology. Wiley, Chichester/Hoboken
9. Pedrini G, Gaspar J, Paul O, Osten W (2009) Measurement of in-plane deformations of microsystems by digital holography and speckle interferometry. Chin Opt Lett 7(12):1109–1112
10. Seebacher S, Osten W, Baumbach T, Jptner W (2001) The determination of material parameters of microcomponents using digital holography. Opt Lasers Eng 36(2):103–126
11. Singh VR, Hedge G, Asundi AK (2006) Digital in-line holography for dynamic micrometrology. In: Proceedings of the optical micro- and nanometrology in manufacturing technology, Strasbourg, 5–7 April 2006, pp 618803–618803-9
12. Singh VR, Miao J, Wang Z, Hegde G, Asundi A (2007) Dynamic characterization of MEMS diaphragm using time averaged in-line digital holography. Opt Commun 280(2):285–290
13. Paul Kumar U, Krishna Mohan N, Kothiyal M (2011) Measurement of static and vibrating microsystems using microscopic TV holography. Opt Int J Light Electron Opt 122(1):49–54
14. Zhang W-M, Tabata O, Tsuchiya T, Meng G (2011) Noise-induced chaos in the electrostatically actuated MEMS resonators. Phys Lett A 375(32):2903–2910
15. Siewe MS, Hegazy UH (2011) Homoclinic bifurcation and chaos control in MEMS resonators. Appl Math Model 35(12):5533–5552
16. Haghighi HS, Markazi AH (2010) Chaos prediction and control in MEMS resonators. Commun Nonlinear Sci Numer Simul 15(10):3091–3099
17. Lin W, Qiao N, Yuying H (2006) Bifurcations and chaos in a forced cantilever system with impacts. J Sound Vib 296(4–5):1068–1078
18. Battiston F, Ramseyer J-P, Lang H, Baller M, Gerber C, Gimzewski J, Meyer E, Gntherodt H-J (2001) A chemical sensor based on a microfabricated cantilever array with simultaneous resonance-frequency and bending readout. Sens Actuators B Chem 77(1–2):122–131
19. Vest CM (1979) Holographic interferometry. Wiley series in pure and applied optics. Wiley, New York
20. Voiculescu I, Zaghloul M, McGill R, Houser E, Fedder G (2005) Electrostatically actuated resonant microcantilever beam in CMOS technology for the detection of chemical weapons. IEEE Sens J 5(4):641–647
21. Ragulskis M, Sanjuan M, Saunoriene L (2007) Applicability of time-average moire techniques for chaotic oscillations. Phys Rev E 76(3):036208